

SPACE-PLANES AND LAUNCHERS AERODYNAMIC STUDY WITH EULER AND NAVIER-STOKES COMPUTATIONS

J. Oswald, J.M. Bousquet

ONERA BP 72, 92322 Châtillon Cedex, FRANCE

ABSTRACT

ONERA has been involved these last years in research activities for space planes and launchers in the framework of the Hermes and Ariane 5 programs. Concerning aerodynamics, one of the main topic was the improvement of the hypersonic and supersonic numerical tools. The purpose of this paper is to describe the capability of the FLU3M code, developed at ONERA, to analyse the aerodynamic characteristics of space planes as well as launchers. The accuracy of the method is assessed by comparison with experimental data. For global forces and moments prediction the Euler solution is used. The chimera technique which reduces significantly the time for grid generation is also used for supersonic applications on Ariane 5 during the separation stage. The Navier-Stokes solutions are preferred when flow recirculation and heat rate are investigated. For the highest velocities, the perfect gas hypothesis is replaced by a chemical equilibrium air model. Laminar applications have been performed on the Ariane 5 launcher, and in the hypersonic regime on the hyperboloid-flare (windward centreline of a re-entry vehicle), on Hermes and on Halis.

INTRODUCTION

Among the critical issues which need to be addressed during the design of space transportation vehicles, one can mention on the aerodynamic side the stability of the launcher during the ascent and control effectiveness of space-planes during atmospheric re-entry ; surface heating on the whole trajectory has to be checked. As long as the prediction of aerodynamic overall forces and moments is needed, the Euler equations may be used in supersonic and hypersonic flow conditions. When accurate predictions of flow patterns and heat fluxes are required on the body surface and around control devices, the viscous effects are to be taken into account since both the flow patterns and the heat fluxes are strongly dependent on surface friction and flow phenomena such as separation, recirculation and reattachment. These structures are also depending on

freestream conditions, especially when high temperature levels are encountered in the flow field. In this case, the air is assumed to be in chemical equilibrium. In order to simulate this effect in computation, the perfect gas state equation is replaced by tables.

Following numerous Euler computations⁽¹⁾ on complete configurations (Hermes, Ariane 5) by using multiblock grids, the need of simplified grid generation process for aerodynamic applications has led to the evaluation of the chimera technique at the applied aerodynamics department at ONERA. This technique has proven to be very efficient when applied to the study of a booster separation as presented in the first part of this paper.

A number of viscous hypersonic simulations with perfect or real gas models were performed in order to investigate the effect of control devices on the flow around vehicles. Typical applications are the supersonic flows around Ariane 5 during ascent with account of propulsion jets from main engine and boosters and the hypersonic flows around re-entry vehicles. For this latter examples, the configurations which were investigated are of varying level of complexity ranging from axisymmetrical hyperboloid-flare configurations, simulating the windward centreline of a re-entry vehicle with a deflected body-flap, to complete 3D vehicles with deflected elevons and flaps, including the computation of base region.

CODE PRESENTATION

In the context of Technical Assistance to CNES , the FLU3M code was used extensively in its Euler form to compute inviscid flows around a variety of 3D configurations⁽¹⁾. However, confronted with the growing need to take viscous effects into account, the previously developed laminar Navier-Stokes version of the FLU3M code was used for flow computations on both 2D and 3D configurations⁽²⁾⁽³⁾. For the cases where equilibrium air simulation is performed, the perfect gas equation is replaced by tables⁽⁴⁾. The main

features of the version of the FLU3M code used for the present computations are :

- A multiblock solver
- A cell-centred formulation
- A "M.U.S.C.L." (Monotonic Upstream Scheme for Conservation Law) approach for the inviscid terms associated with a Van Albada limiter
- A central discretisation for the viscous terms
- A Flux Difference Splitting of Roe with a Harten entropy correction. The modification defined by Glaister⁽⁵⁾ is used for equilibrium air computations.
- A viscosity defined by the classical Sutherland law for perfect gas
- A Van Leer implicit for perfect gas and a Linearised Conservative Implicit⁽⁶⁾ for equilibrium air, both associated with a triple ADI (Alternate Direction Implicit) acceleration technique.
- Isothermal and zero pressure gradient wall boundary conditions
- A chimera option for computation of overlapping grids.

ARIANE 5

FLU3M computations were carried out on the Ariane 5 launcher, in the frame of Technical Assistance to CNES. The aim of these computations is two folds : on one hand, to analyse the global aerodynamic force and moment coefficients and on the other hand, to describe the flow structure around the launcher in particular at the rear where propulsion jet flows interact with the base flow.

To illustrate the use of the Euler option of FLU3M, one has selected the case of a booster separation, from the central body. For each position of the booster, a new grid has to be constructed. A classical 3D grid for this type of application is presented in figure 1. In this case, the booster is separated laterally of 8.5m and backward of 3.2m, with no sideslip $\beta=0^\circ$. Although the multiblock technique is used, the construction of such a new grid for a new position of the booster was found expensive, for that reason the chimera technique was used. This technique allows to generate separately and easily the booster mesh and the central body mesh. Special boundary conditions enable the transmission of the information at the external boundary of one mesh inside the other mesh and to take account of the body into the other mesh. The 3D chimera grid created for the same application is presented in figure 2. The Mach

number contours of the Euler computation on this application at Mach 5.5 are presented in figure 3 for the classical method and in figure 4 for the chimera method. One can notice the good agreement between those two results in the shock representation. The interaction of the bow shock from the central body with the bow shock from the booster is captured with the same accuracy in both computations. The chimera technique was used to compute five different sideslip angle of the booster -20° , -10° , -5° , 0° and 5° with the same location of the centre of gravity of the booster. The same meshes were used for these five computations. The lateral force and the yaw moment are the interesting coefficients to analyse during the separation stage. The computed lateral force and yaw moment coefficients at the centre of gravity are compared in figure 5 and 6, with those measured in the S3MA ONERA wind-tunnel. The results of two classical computations carried out on two different grids with $\beta = -20^\circ$ and 0° are added. One can notice that the agreement between the chimera computations, the classical computations and the experiment is good.

The detailed analysis of the flows around the Ariane 5 launcher requires the account of the full 3D geometry including the effect of the propulsion jets. Some previous calculations were carried out with the Euler solver. For the presented computation, the viscosity of the flow is taken into account at a lower Reynolds number than in flight, closer to S3MA wind tunnel conditions. The Reynolds number is $1.6 \cdot 10^6$ based on the diameter of the body ; a laminar viscosity is assumed following Sutherland laws. The jet conditions were defined by applying a Goethert similarity rule which enables a hot jet to be simulated by a cold one. The aerodynamic conditions are summarised in the following table :

	Mach	Pi (bar)	T (K)	P_j/P_∞
Free stream	3.5	5.62	99.25	
Central jet	4.56	108.0	57.1	4.76
Booster	2.80	114.8	114.8	12.80

For the present computation no incidence and no sideslip is considered. This allows, due to the double symmetry created to mesh only a quarter of the configuration. Twelve blocks were necessary to create the mesh which amounts about 1 million grid points. The normal to the wall first cell size is equal to $\Delta\eta/L_{ref}=16.6\mu\text{m}$. The mesh in the plane of symmetry of the booster and on the body are presented in figure 7. One can notice the dark regions which correspond to the clusterisation of the points near the wall, especially

between the two bodies and in the base region. Two computations were carried out on the fine grid (1S1) and on the medium grid (1S2 : by keeping one point over two in each direction). The pressure contours on the body and in the symmetry plane of the boosters from both computations are presented in figure 8. The global features of the flow field are the same. One can clearly see the capture of the bow shocks issued from the fore body and from the conical part of the booster. There is clearly an interaction of the booster bow shock with the central body boundary-layer. At the rear, a complex flow structure takes place in the area between the central body base region, the booster and the jet plumes where shock shock interactions occur. Some differences can be noticed in the capture of the shocks from the medium grid computation and in the fine grid computation. A detailed view of the Mach number contours in the rear flow is presented in figure 9. One clearly sees the mixing zones between the expanding jets and outer flows at the booster end, as well as the complex shocks and slip-lines interactions downstream of the jet exhausts. These features indicate the highly three dimensional character of the flow structure in the base region. In the symmetry plane of the booster the pressure coefficient distribution is presented in figure 10. For a clarity purpose, the pressure coefficient of the booster were shifted of +0.25. On the central body, one can see the interaction of the booster bow shock. This interaction creates an upstream recirculation in the boundary layer represented by the bump in front of the pressure peak. On the external generatrix of the booster, the compression of the conical nose is followed by a sharp expansion at the junction with the cylindrical part of the booster. At the rear, in the base region there is a decrease of the pressure on the central body and on the internal generatrix of the booster. In figure 11, the computed pressure coefficients on the a booster generatrix perpendicular to the booster symmetry plane are compared with experimental measurements obtained in the S3MA ONERA wind tunnel. The main difference is at the rear in the base region where the simplifications done on the geometry and the viscous model may explain these differences. The agreement between computations and test on the booster cylindrical part is nevertheless good.

As a conclusion the chimera method is well suited for a study of global coefficients during a separation stage. For the detailed analysis of flow structures, the laminar computation on the whole Ariane 5 geometry plus booster with account of jets has proven successful which is a first step for carrying out in a near future a turbulent computation on this configuration.

HYPERBOLOID-FLARE

In order to study blunt re-entry vehicles in hypersonics, it was decided to start with an axisymmetric geometry which provided a way of studying simple configuration closer to 3D geometry than 2D cases are. Such a geometry was created by rotating the windward centreline of Hermes 1.0 (30° incidence, 13.6° flap deflection) around the flow axis. This hyperboloid-flare test case was used to validate the FLU3M method with experimental results obtained in the ONERA R5Ch and R3Ch wind tunnels. The flow conditions for the two computations are given in the table below:

Tunnel	Mach	Re	\bar{V}
R5Ch	9.95	11414	0.093
R3Ch	9.56	120000	0.028

The R5Ch conditions correspond to a high value of viscous interaction parameter, defined as $\bar{V} = M / \sqrt{\text{Re}}$. The Reynolds number Re is based on the overall length of the hyperboloid-flare. For both computations the wall temperature is 300 K. For the computations under R5Ch conditions, grid convergence is achieved by obtaining identical flow results on 201x77 and 401x153 grids. In the R3Ch conditions, the grid convergence is achieved on 201x97 and 401x193 grids.

The agreement of the computation result with wind tunnel results is excellent, as can be seen on figure 12 where computed density contours are compared to experimental shock structures obtained with an Electron Beam Fluorescence (EBF) technique.

The computed pressure coefficient are compared to those measured in experiment in figure 13. The results are in very good agreement for both flow conditions. The plateau level and the separation length for R3Ch conditions are particularly well predicted by the computation.

The comparison of heat flux levels is carried out by means of the Stanton number as defined by Miller which enables the reduction of laminar flow data obtained in different hypersonic flow conditions. The results from computation and experiment, for both flow conditions, are compared in figure 14. The results are generally in very good agreement, particularly in the region of separated flow where heat flux levels are accurately predicted. Also well predicted are the increase in heat flux levels before reattachment and the separation lengths, with the computations giving slightly larger lengths than the experiments.

Detailed analysis of the computed Mach number contours in the R5Ch conditions (figure 15-a), shows that a small separation zone appears in the hinge line region, where a shock structure is generated. This shock is in fact composed of a separation shock and a reattachment shock, both of which focus with the bow shock into a triple point.

The higher Reynolds number for the R3Ch conditions meant that the density of the R5Ch grid had to be increased in the normal direction and that grid points had to be clustered near the wall. The shock structure (figure 15-b) is modified by the increase of the recirculation zone. The separation shock interacts strongly with the bow shock, with a slight deviation of the resulting shock which interacts downstream with the reattachment shock.

The first application of the FLU3M code with the real gas model⁽⁴⁾ is carried out on the same hyperboloid-flare configuration. The aerodynamic conditions are $M=25$, $\rho_{\infty}=3.2 \cdot 10^{-5}$, $T_{\infty}=192.K$ and $T_w=800.K$ which gives a Reynolds number of $2.21 \cdot 10^5$ for a reference length of 12.916m.

The global features of the flow field are presented in figure 15-c (Mach numbers contours). The bow shock is closer to the surface of the hyperboloid than in the perfect gas cases and the separation zone is very small. The three shocks in the recirculation zone are differently placed than those previously presented. Due to the smaller recirculation zone, there is first an interaction between the separation shock with the reattachment shock, near the hinge line. Then the bow shock interacts with the reattachment shock.

In figure 16, the computed real gas pressure coefficient distributions are compared with the computed perfect gas coefficient in R3Ch conditions. The two simulations are carried out at nearly the same Reynolds number. The pressure level decrease on the hyperboloid is the same, whereas the maximum pressure level is higher on the flare with the real gas model. The pressure plateau length is directly linked to the recirculation extent, which is small in the real gas case.

In conclusion, the excellent comparisons between experiment and computation validates the FLU3M code for applications on axisymmetric shapes, for which grid convergence studies are obtainable. The extension to real gas simulation contributes to the qualification of the method for 3D applications

HERMES

Two aerodynamic conditions were investigated with the Navier-Stokes solver on the three dimensional

Hermes 1.0 geometry : one corresponding to S4MA wind tunnel conditions (Mach = 10, $T_{\infty}= 52.K$, $Re = 2.1 \cdot 10^6$) and the other corresponding to a flight test case ($H = 77.Km$, Mach = 25, $T_{\infty} = 203.6K$, $Re = 3.5 \cdot 10^5$). Each aerodynamic condition was computed with and without the 10° of body-flap and elevon deflection, and at an angle of attack of 30° . The first computation was carried out with a wall temperature of 300.K and a perfect gas model, while the second specified a wall temperature of $T_w = 1300.K$ and an equilibrium air model⁽⁴⁾. The geometry of Hermes was simplified in that the slots between flaps were filled and the body-flap was truncated at the rear of the fuselage. The meshes used for the two aerodynamic conditions are shown in figure 17. Due to the XZ symmetry, only half the configuration was computed, amounting to approximately 1 million points.

In a first step, the perfect gas computation results are compared to wind tunnel results.

On the leeward side, the comparison between computed streamlines and S4MA oil flow visualisations (figure 18) shows that the computation successfully predicts two long separation lines, on the wing and on the fuselage, which are clearly visible on the oil flow visualisations. Similarly, the complex recirculation at the bottom of the canopy apparent in the experiment is well resolved by the computation.

The Stanton Miller number is used to compare the computed heat fluxes with those measured experimentally at different Reynolds numbers. Figure 19 shows the computed and measured Stanton Miller numbers in an XZ plane through the external side of the elevon, for the flap deflected configuration. There is some discrepancy between the values, but the overall Stanton Miller levels are comparable and the results show similar general trends. The noticeable difference between experimental values suggests that the flow for run 1271 may not be fully laminar close to trailing edge of the elevon. Also, it should be noted that the number of measurement points is insufficient to be able to evaluate the fluctuations which are predicted by the computation.

In figure 20, the presentation of the Mach number contours in the rear plane points out the real gas effects on the flow field structure. The perfect gas features of a flow field which Mach number are greater than 10, are very similar. This enables to investigate real gas effect by comparing computation at Mach 10 with perfect gas and at Mach 25 with real gas. The bow shock computed with the perfect gas model is about twice farther from the windward surface than these computed with the real gas assumption.

The windward pressure coefficients obtained with the perfect gas simulation for the flaps deflected configuration are shown in figure 21-b. The stagnation point and the compression on the body-flap and the

elevons are well resolved, as are the expansions along the wing leading edge and outboard edge of the elevon.

The wall streamlines on the windward side (body-flap and elevon deflected of 10°) are presented in figure 22-b. Each deflected control surface can be seen to generate an area of flow recirculation around the hinge line. For the elevon the recirculation is actually a double recirculation.

The windward pressure coefficients obtained with the Mach=25 real gas computation on the flaps deflected configuration, are shown in figure 21-a. The general features are similar to those obtained at Mach=10 (figure 21-b), with, however, a slight shift in pressure level, the pressure coefficients at a given point on the windward side being somewhat higher for the real gas computation. The flow recirculations computed at Mach 25 (figure 22-a) are small over the body-flap hinge and inexistant over the elevon. The real gas computation considerably decreases the recirculation structure and the pressure gradients generated by the deflection of the flaps are stronger.

The pressure coefficient distribution on the windward centreline at Mach 10 only differs from these at Mach 25 (figure 23) in the recirculation zone. The agreement between the two curves is good before and after the body-flap hinge where the recirculation takes place. In the perfect gas case, a plateau pressure corresponds to the large recirculation extent, whereas no plateau can be seen in the real gas case, where the recirculation extent is small (figure 22).

In conclusion, the 3D computations performed on Hermes 1.0 have shown that the FLU3M Navier-Stokes method successfully resolves complex 3D flow structures such as separations and recirculations, with perfect or real gas model, on both the windward and leeward sides of the vehicle.

HALIS

The Halis geometry was essentially the windward side of the US space shuttle orbiter with a simplified leeward side (no canopy, no tail fin, ...). The resulting geometry is simpler to mesh and to compute while the windward side retains the features of interest of the US orbiter. The configuration which was computed corresponds to the S4MA wind tunnel conditions (Mach = 9.8, $T_{i\infty} = 1100.K$, $P_{i\infty} = 25bar$, $Re = 6.1 \cdot 10^5$). The wall temperature is 300.K and the reference length is 32.77m. The angle of attack is 40° and the body-flap is deflected of 15° . Due to the XZ symmetry, only half the configuration was computed, amounting to approximately 2.7 million grid points. One of the particularity of this computation is that the base region

was entirely meshed in order to properly account for the suction of this area on the flow recirculation on the flap. In the following the results of the two computations carried out on the fine grid (1S1) and on the medium grid (1S2 : keeping one point over two in each direction) are presented.

In figure 24, the Mach number contours (fine grid computation) on the body and in the symmetry plane are presented. The bow shock is sharply captured even at the leeward side. One notices the trace of the classical separation and reattachment shock on the deflected flap and the strong expansion at the rear of the flap.

The pressure coefficient contours on the windward side are compared in figure 25. One can notice that the pressure levels are in close agreement on fine grid and on medium grid. In the flap area, only slight differences can be seen in the constant pressure zone induced by the large separation extent. The detailed view of the wall streamlines in the recirculation area on the flap (figure 26) shows the very large extent and the strongly 3D structure of the recirculation. A stable double recirculation structure is captured in the medium grid computation. The result on the fine grid shows a larger extent of the primary recirculation and a more complex shape of the secondary recirculation which may be affected by some instability of the flow at reattachment.

The comparison of the computed pressure coefficient with S4MA measurements in figure 27, shows a good agreement in the front part of the vehicle. The recirculation zone starts at the same location $X/L = 0.8$ in computations and in experiment. Downstream, the pressure plateau and the pressure peak at reattachment are in better agreement with experiment in the medium grid result than in the fine grid result.

In figure 28, the computed Stanton number in the rear windward centreline is compared to S4MA data. In front of the recirculation ($X/L < 0.8$), the computed level are slightly higher than the experimental one. The decrease of the Stanton number which corresponds to the recirculation area has the same extent in computation and in experiment. One can notice that the measured heating rate at reattachment on the rear part of the body flap is exactly matched by the medium grid result.

As a conclusion, the very good agreement between the medium and the fine grid results especially on the fore body assesses the high level of grid convergence of the computations. The Halis 3D computation shows the robustness of the code to compute complex flow structures even if the density level are very low (base region and leeward side), and the accuracy of the scheme for the prediction of flap efficiency and heating rates.

CONCLUSION

The FLU3M code has been extensively used under supersonic and hypersonic flow conditions encountered by spacecraft and launchers.

As long as overall aerodynamic coefficients are studied, the reference 1 has shown that the Euler option of the method is efficient on launchers or on spacecraft configurations. The present use of the chimera option allows a larger flexibility in grid construction when the geometry is complex and moving as in a booster separation case, while keeping a good accuracy in the results.

For a precise evaluation of the flow structures including recirculation zones, the Navier-Stokes option of the FLU3M method is used. At first, computations on axisymmetric configurations provided results which were found to be in very good agreement with experiment. In addition, the relatively moderate size of these configurations enabled grid sensitivity studies to be conducted. These showed that the computations were nearly grid independent. In addition the extension to real gas computation simulating flight conditions has increased the application range of the solver. Such accurate results validated the FLU3M method for axisymmetric configurations, and qualified the method for 3D applications. The 3D FLU3M computations on the Hermes 1.0 configuration (for perfect gas and real gas) and Halis or Ariane 5 configuration (perfect gas only), showed that the method provided accurate predictions of complex flow structures, such as flow separations and recirculations, on the windward and leeward sides and base region of the vehicle. The real gas effect on those structures can also be investigated with this code. This is of particular importance since the effectiveness of control devices such as flaps and elevons is controlled to a large extent by these structures. Furthermore, concerning the pressure and heat flux predictions, it was found that further comparisons were nonetheless necessary to fully validate the method, underlining the present need for additional representative 3D experimental data.

Future activities will be devoted to a better account of turbulence models which have to be considered when the flow conditions in supersonic flight is no more laminar.

ACKNOWLEDGEMENTS :

The present study was partially funded by CNES (the French Space Agency) and ESA (European Space Agency).

REFERENCES

- [1] J.M. BOUSQUET, R. COLLERCANDY, L. DALA, A. DEMARGNE, J. OSWALD. Computational methods applied to the aerodynamics of space planes and launchers, ICAS 92 (4.3.4.) Beijing (China), September 20-25, 1992 .
- [2] J. OSWALD, A. DEMARGNE, J-M. BOUSQUET. Hypersonic laminar computations of separated flows with account of real gas effects, AIAA 95-2271- San Diego (USA), June 1995.
- [3] J. OSWALD, C. JOUET , Ph. GUILLEN. Etudes des écoulements hypersoniques laminares à l'aide du code FLU3M, AAAF - 9 Nantes (France), 25-27 octobre 1993.
- [4] M. GAZAIX. Hypersonic inviscid and viscous flow computations with a new optimized thermodynamic equilibrium model, AIAA Reno, NV (USA), January 1993.
- [5] P. GLAISTER. An approximate linearised Riemann solver for the Euler equation for real gases, J. Comput. Phys, 74, 382 (1988).
- [6] H.C. YEE, A. HARTEN. Implicit TVD schemes for hyperbolic conservation laws in curvilinear coordinates, AIAA 1513 Cincinnati Ohio (USA), July 15-17, 1985.

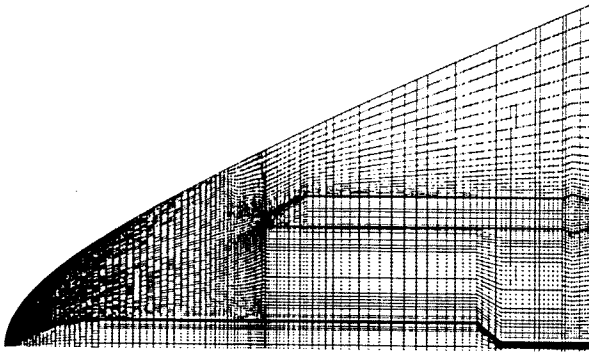


Figure 1 : Classical 3D grid around the booster separated from Ariane 5 for Euler computation (131 000 grid points).

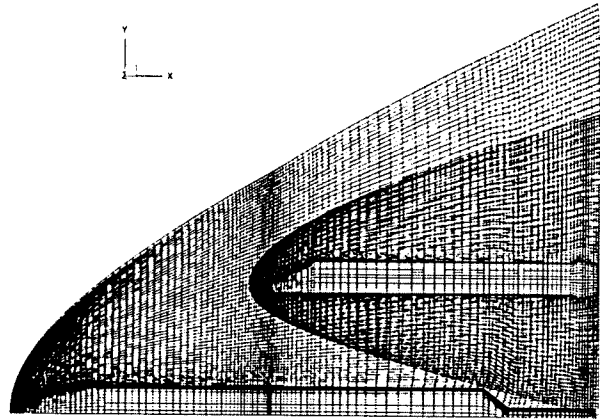


Figure 2 : Chimera 3D grid around the booster separated from Ariane 5 for Euler computation (173 000 grid points).

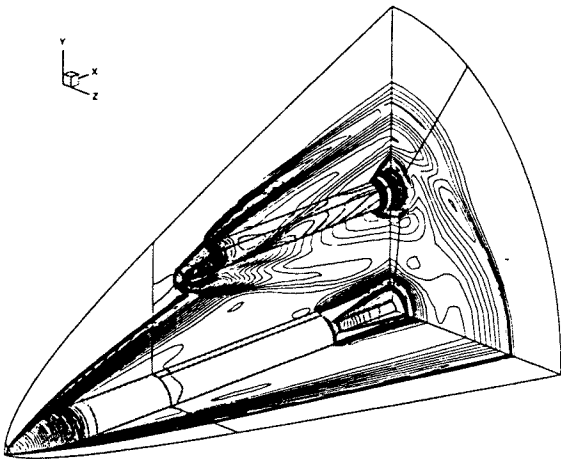


Figure 3 : Ariane 5 + booster Euler FLU3M computation - classical technique - pressure contours in the symmetry planes and on the body - $M=5.5$

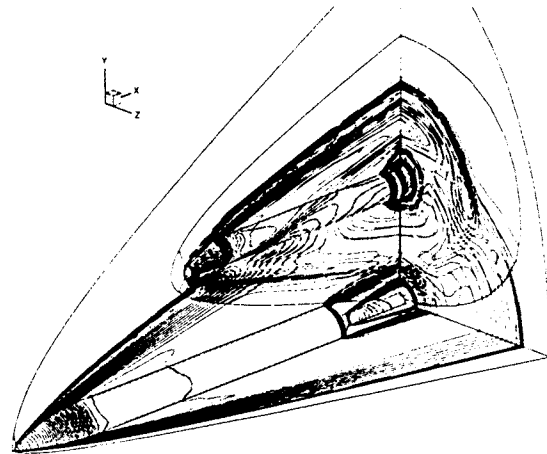


Figure 4 : Ariane 5 + booster Euler FLU3M computation - chimera technique - pressure contours in the symmetry planes and on the body - $M=5.5$

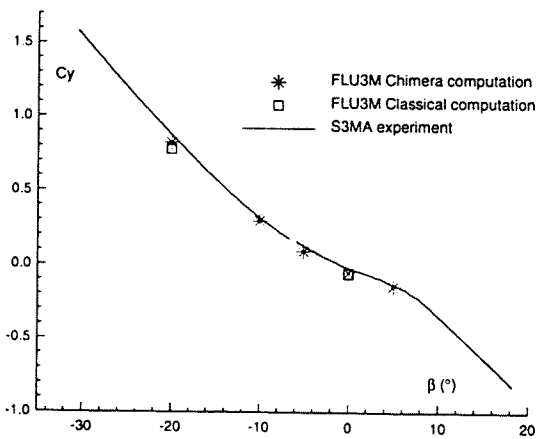


Figure 5 : Comparison of FLU3M chimera computation with FLU3M classical computation and with S3MA experiments on booster lateral force coefficient.

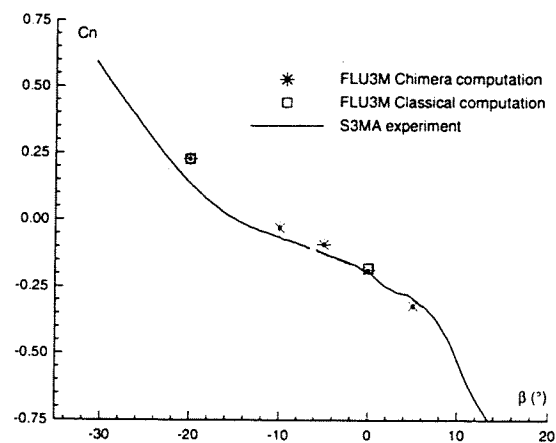


Figure 6 : Comparison of FLU3M chimera computation with FLU3M classical computation and with S3MA experiments on booster yaw moment coefficient (reference at centre of gravity).

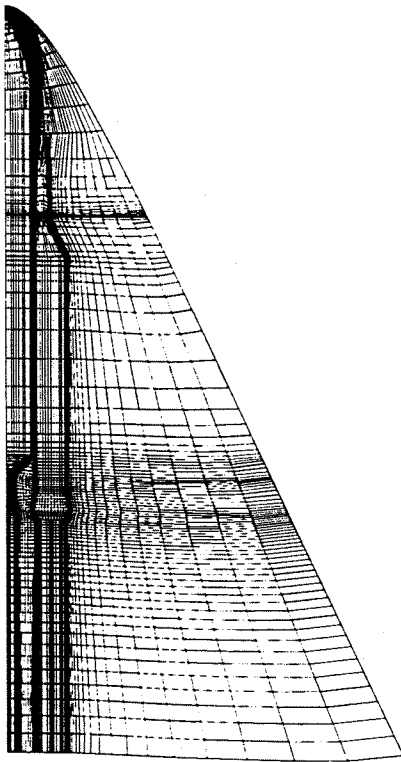


Figure 7 : Classical 3D grid around Ariane 5 + booster for Navier-Stokes computation (1 million of grid points).

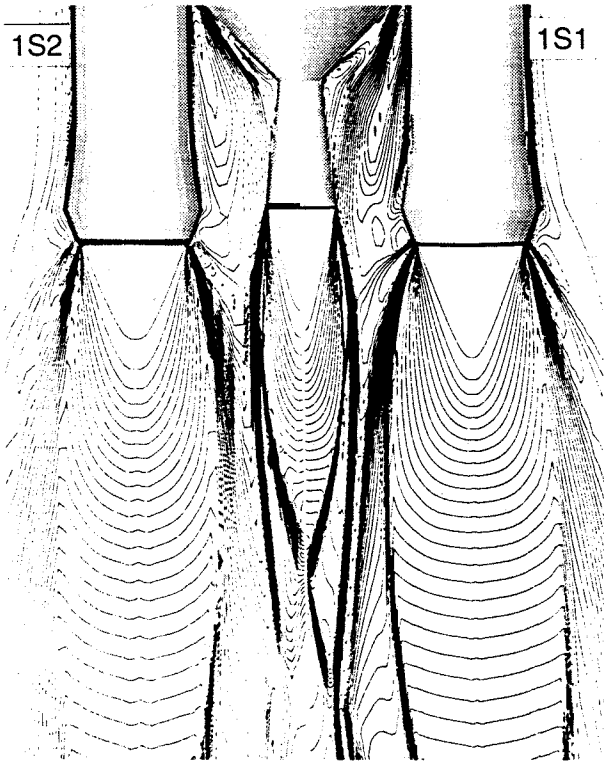


Figure 9 : Comparison of computed Mach number contours in the base region of Ariane 5 + booster + jets - left medium grid computation (1S2), right fine grid computation (1S1) - $M=3.5$ $Re=1.59 \cdot 10^6$ $T_\infty=99.K$ $T_w=300.K$ $\alpha=0^\circ$

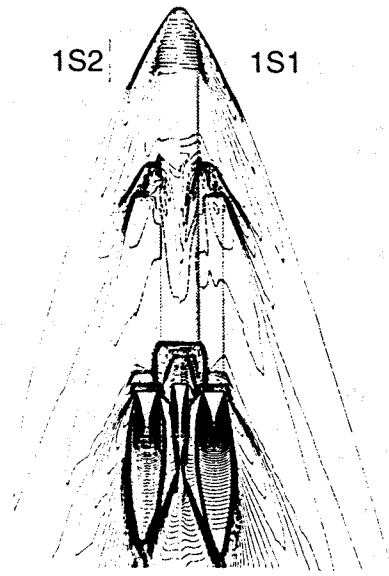


Figure 8 : Comparison of computed pressure contours on Ariane 5 + booster + jets - left medium grid computation (1S2), right fine grid computation (1S1) - $M=3.5$ $Re=1.59 \cdot 10^6$ $T_\infty=99.K$ $T_w=300.K$ $\alpha=0^\circ$

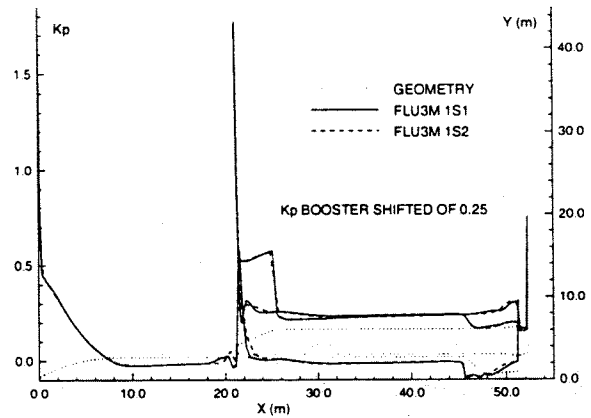


Figure 10 : Comparison of pressure coefficient distributions on the symmetry plane of Ariane 5 + booster - medium grid and fine grid computations.

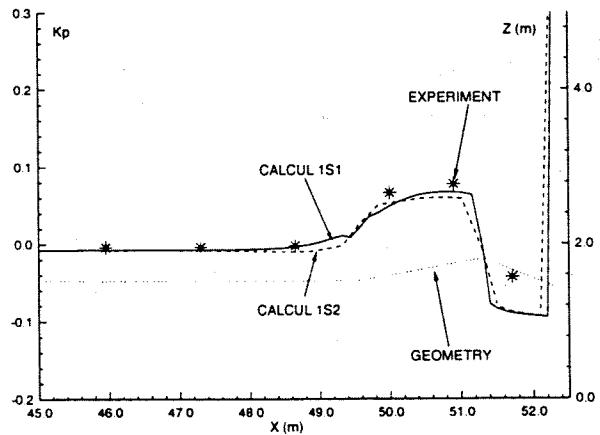


Figure 11 : Comparison of FLU3M medium grid and fine grid computations on a booster generatrix with S3MA experiments - pressure coefficient distributions on the symmetry plane of Ariane 5 + booster

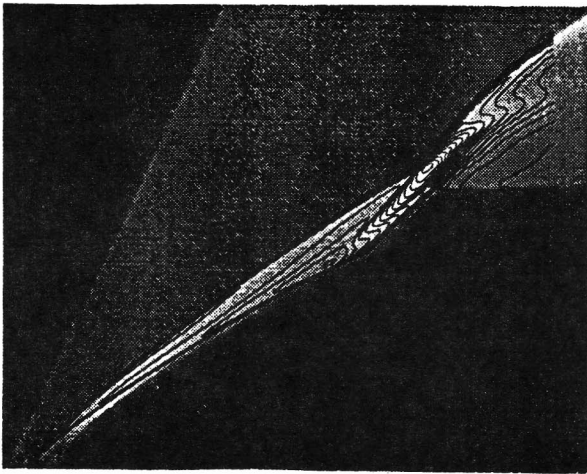


Figure 12 : Comparison of FLU3M computation (density contours) on the hyperboloid-flare with R5Ch Electron Beam Fluorescence visualisation technique.

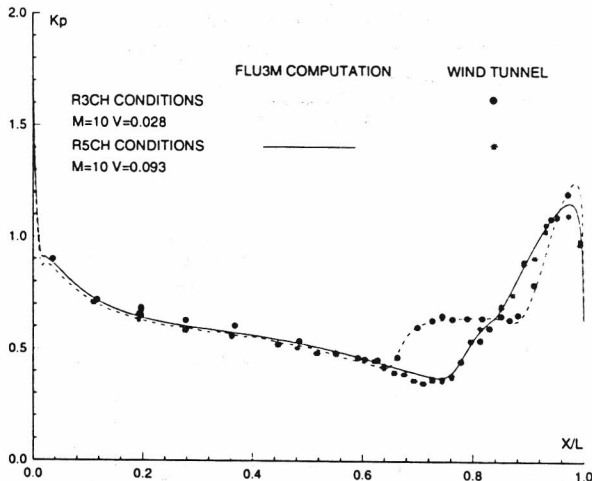


Figure 13 : Comparison of FLU3M computation on the hyperboloid-flare with R5Ch and R3Ch experiments - pressure coefficient distribution.

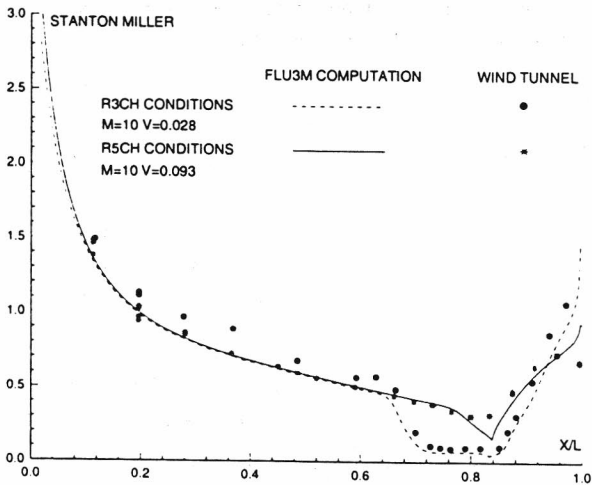


Figure 14 : Comparison of FLU3M computation on the hyperboloid-flare with R5Ch and R3Ch experiments - Stanton Miller coefficient distribution.

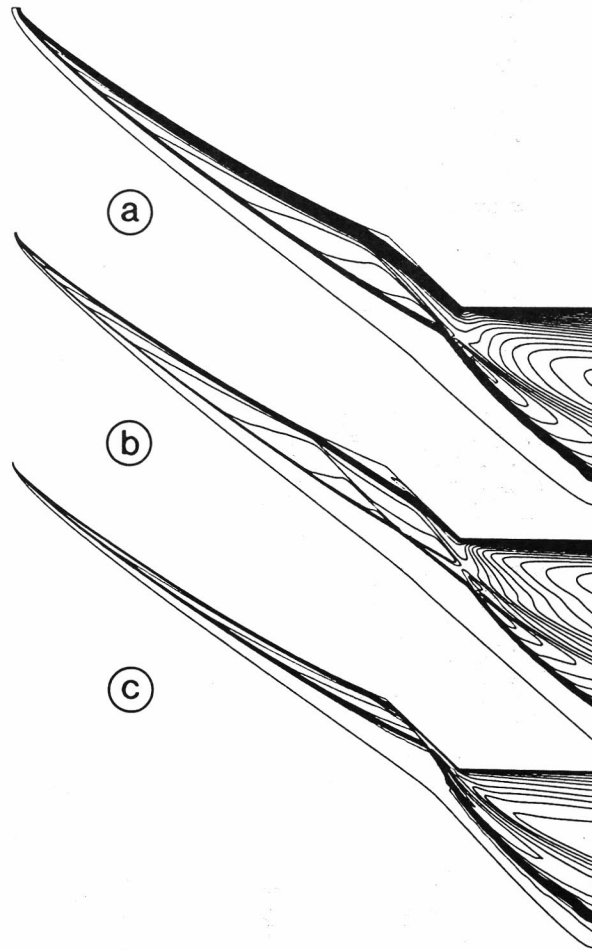


Figure 15 : Mach number contours around the hyperboloid-flare a) perfect gas computation - R5Ch conditions - $M=10$ $Re=11414$ $T_\infty=52.K$ $T_w=300.K$ b) perfect gas computation - S4MA conditions - $M=10$ $Re=2.21 \cdot 10^5$ $T_\infty=52.K$ $T_w=300.K$ c) real gas computation - $M=25$ $Re=2.251 \cdot 10^5$ $T_\infty=192.K$ $T_w=800.K$

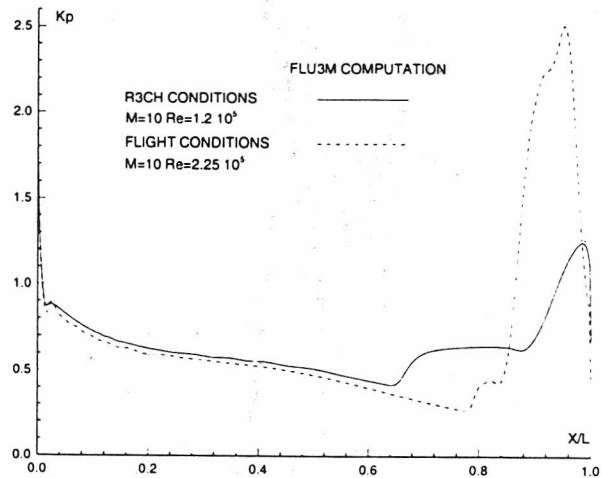


Figure 16 : Comparison of pressure coefficient distributions on the hyperboloid-flare - perfect gas and real gas computations.

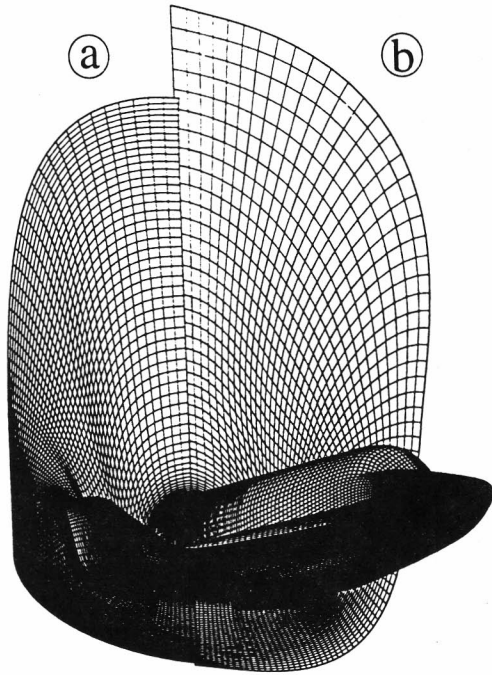


Figure 17 : Comparison of 3D grids around Hermes 1.0 (rear plane and body surface) for a) real gas and b) perfect gas computation.

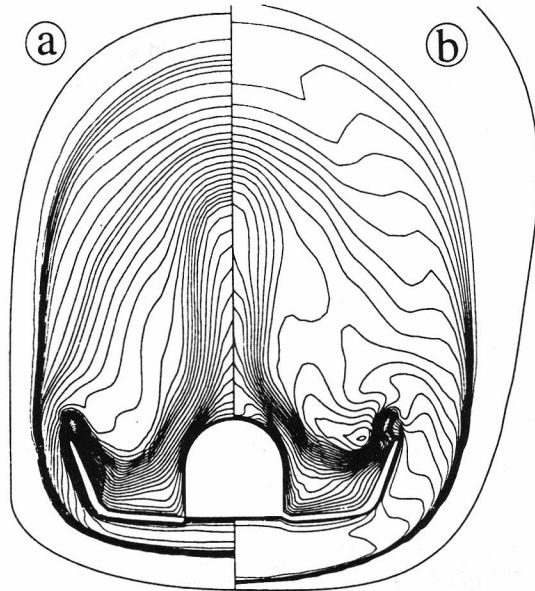


Figure 20 : Comparison of computed Mach number contours in the rear plane of Hermes 1.0 ($\alpha=30^\circ$) a) Mach 25 (real gas) and b) Mach 10 (perfect gas).

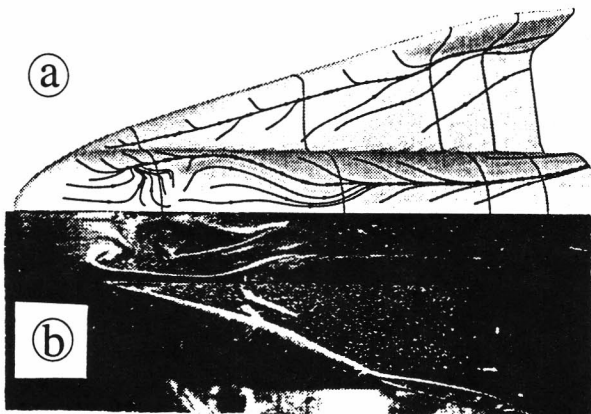


Figure 18 : Comparison of a) FLU3M computation on Hermes 1.0 ($\alpha=30^\circ$) leeward side (wall streamlines) with b) oil flow visualisation in S4MA.

- FLU3M $Re=2.1 \cdot 10^6$
- S4MA RUN 1271 $P_i=84.2\text{bar}$ $Re=2.13 \cdot 10^6$
- S4MA RUN 1307 $P_i=24.9\text{bar}$ $Re=0.65 \cdot 10^6$

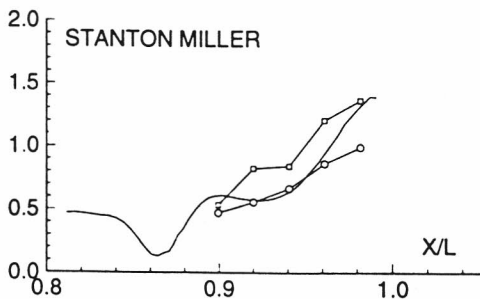


Figure 19 : Comparison of FLU3M computation on the elevon ($Y/L=0.114$) with S4MA experiments - Stanton Miller coefficient.

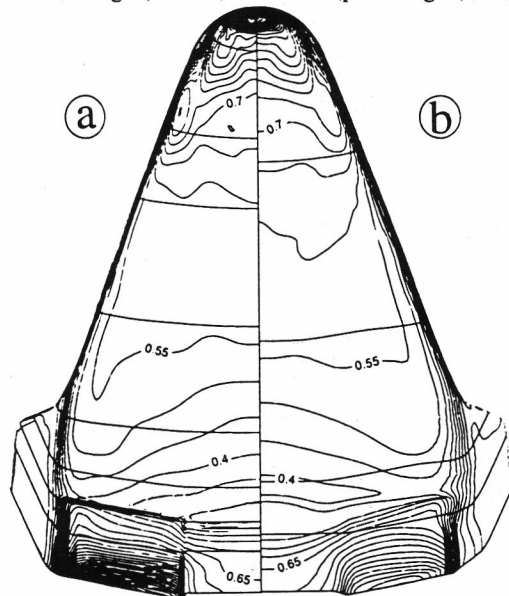


Figure 21 : Comparison of computed pressure coefficient on Hermes 1.0 ($\alpha=30^\circ$) windward side with body-flap and elevon deflected 10° a) Mach 25 (real gas) and b) Mach 10 (perfect gas).

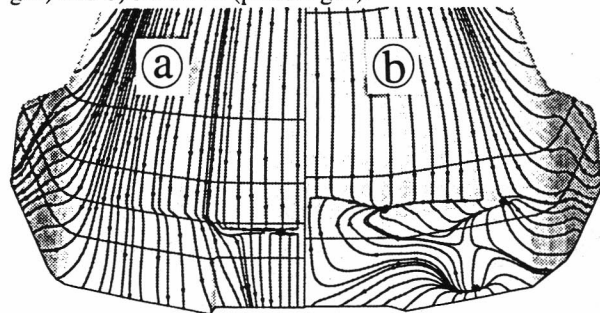


Figure 22 : Comparison of computed wall streamlines on Hermes 1.0 ($\alpha=30^\circ$) windward side with body-flap and elevon deflected 10° a) Mach 25 (real gas) and b) Mach 10 (perfect gas).

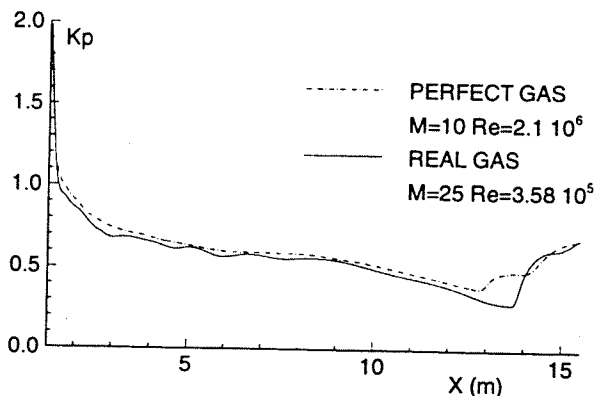


Figure 23 : Comparison of pressure coefficient distributions on the windward centreline of Hermes 1.0 - real gas and perfect gas computations.

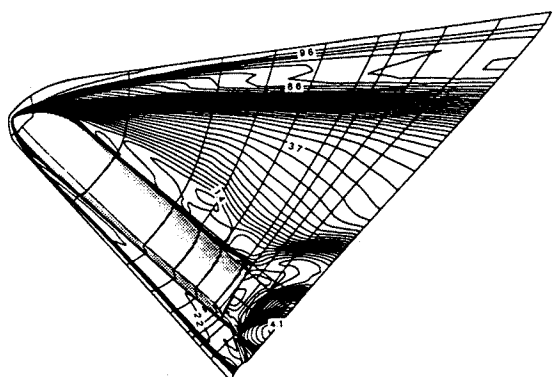


Figure 24 : Halis FLU3M computation - Mach number contours in the symmetry plane - S4MA conditions - $M=10$ $Re=6.08 \cdot 10^5$ $T_{\infty}=52.K$ $T_w=300.K$ $\alpha=40^\circ$ $\delta_{body-flap}=15^\circ$.

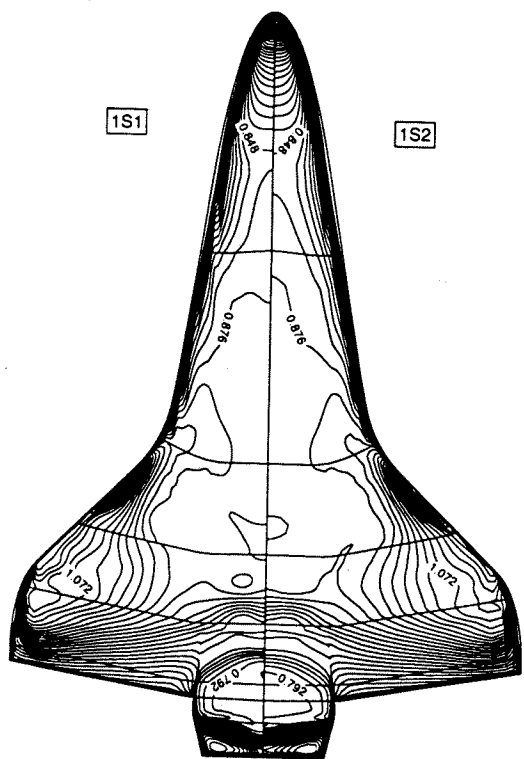


Figure 25 : Comparison of computed pressure coefficient on Halis windward side - right medium grid (1S2), left fine grid (1S1) - S4MA conditions.

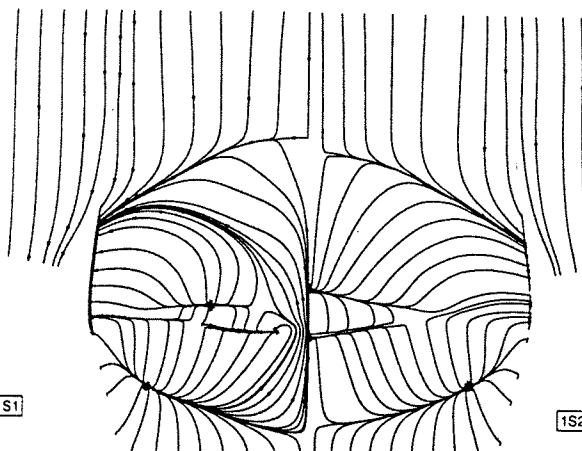


Figure 26 : Comparison of wall streamlines on Halis - detail in the flap region - right medium grid computation (1S2), left fine grid computation (1S1) - S4MA conditions - $M=10$ $Re=6.08 \cdot 10^5$ $T_{\infty}=52.K$ $T_w=300.K$ $\alpha=40^\circ$ $\delta_{body-flap}=15^\circ$.

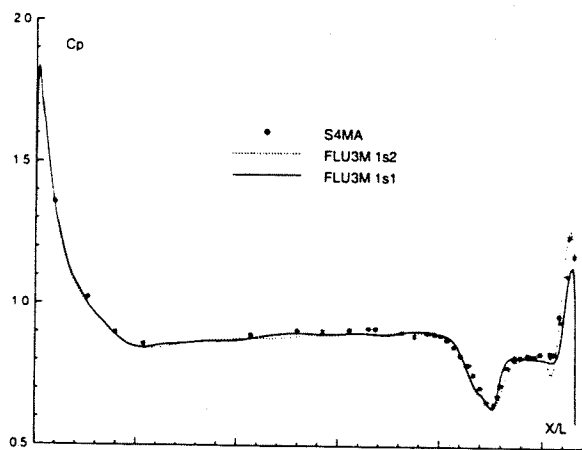


Figure 27 : Comparison of FLU3M medium grid and fine grid computations with S4MA experiment - pressure coefficient distributions on the HALIS windward centreline.

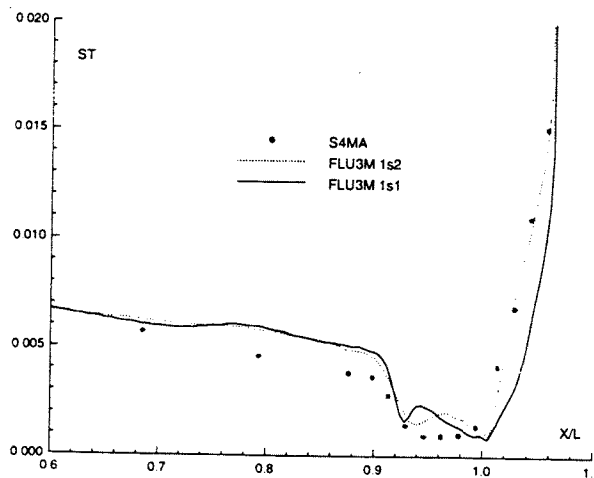


Figure 28 : Comparison of FLU3M medium grid and fine grid computations with S4MA experiment - Stanton number coefficient distributions on the windward centreline (flap area).